Optics & Laser Technology 56 (2014) 278–284

Contents lists available at ScienceDirect

Optics & Laser Technology

journal homepage: www.elsevier.com/locate/optlastec

Low-cost/high-reproducibility flexible sensor based on photonics for strain measuring

R.P. Rocha [a], J.M. Gomes [a], J.P. Carmo [a,*], A.F. Silva [b], J.H. Correia [a]

[a] University of Minho, Department of Industrial Electronics, 4800-058 Guimarães, Portugal
[b] MIT—Portugal, EDAM Program, University of Minho, School of Engineering, 4800-058 Guimaraes, Portugal

ARTICLE INFO

Article history:
Received 25 July 2013
Accepted 25 August 2013
Available online 21 September 2013

Keywords:
Fabrication technology
Flexible sensors
Strain measurement

ABSTRACT

This paper presents a flexible sensor based on photonics for measuring strain, curvatures and vibrations. This flexible sensor is composed by a Fiber Bragg Grating (FBG) embedded into polydimethylsiloxane (PDMS). The selected FBG resonates at the wavelength of 1552.37 nm and is embedded before the curing for enabling a strong adhesion between both components. Few prototypes were fabricated and characterized. The measurements showed a maximum strain sensitivity of $\approx$400 pm per 1% elongation, revealing to be sensitive to strain/bending forces and vibration. The measurements allowed to establish a predictable response for both static and dynamic behavior, corresponding to a resolution of $\approx$88 pm per curvature degree. This flexible sensor also allowed high strain cycles and presented the linear behavior of $\approx$14 pm $^{\circ}C^{-1}$ over the temperature range 20-110 $^{\circ}$C. The high-simplicity of the fabrication process results on low-cost with high-degree of reproducibility of their characteristics.

1. Introduction

Flexible sensors are a very interesting solution for many applications [1]. Since sensors are what translate physical quantities into signals that can be measured, read, characterized and used for actuating purposes, they play a crucial role in everyday life, in a direct and indirect way. Traditionally, the optics has been used trough the history on sensors [2], light sources [3], actuators [4], displays [5] and so on. Therefore, it is not strange the extension of their use within flexible/bendable systems. Biomedical [6], robotics [7,8], textile applications [9] and temperature measurement [10], vibrations [11,12] and accelerations [13] are few of the potential uses for flexible sensors. In this context, the use of Fiber Bragg Gratings (FBGs) is an interesting proposal for implementing flexible sensors [14–16] especially for strain measurement. The ability to accurately measure this physical property is more and more important in the most aspects of daily life [17,18]. However, the task to provide highly-reliable methods is a challenging task. In this context, the optic methods are especially suitable for achieving such a purpose. In this sequence of ideas, this paper presents a flexible sensor based on optics for measuring strain and bend. The PDMS was selected to be the FBG's carrier due to its inherent high flexibility, inert properties, simple mix/cure processes and tolerance to high temperatures. The PDMS also provides excellent sensor adaptation to both wide ranging structure geometries and environment conditions, and at same time, it also works as a protective layer for the FBG. Moreover, the PDMS is not easily tearable and has a nontoxic nature, which means that it is compatible with biomedical applications; therefore, structures made of this material can be directly attached or strapped onto a person [19].

2. FBG embedment in PDMS

2.1. Mold design

Preliminary considerations about the proposed embedment method must be made in order to explain and justify the design of the proposed flexible sensor. The diameters of the optic fiber and FBG measure, respectively, 250 and 125 μm; whereas the length of the FBG is 8 mm. In order to completely embed the FBG within the PDMS, a volumetric cavity, from now on considered as "mold" measuring $65 \times 10 \times 0.9\ mm^3$ ($l \times w \times h$) was designed with the CAD model illustrated in Fig. 1(a). A guide channel, where the optic fiber is placed and hold in place by two holders (also seen in the CAD model), is cut into the mold. The two holders keep the stretched in order to maintain the tension along the entire process, hence guaranteeing that the fiber is centered in the PDMS from one end to the other. This is also certified by the aforementioned guide channel which also guarantees that the center of the optic fiber is kept at the determined depth of 450 μm, more specifically, the center of the cavity.

* Corresponding author. Tel.: +351 253 510190; fax: +351 253 510189.
E-mail address: jcarmo@dei.uminho.pt (J.P. Carmo).

0030-3992/$ - see front matter © 2013 Elsevier Ltd. All rights reserved.
http://dx.doi.org/10.1016/j.optlastec.2013.08.024

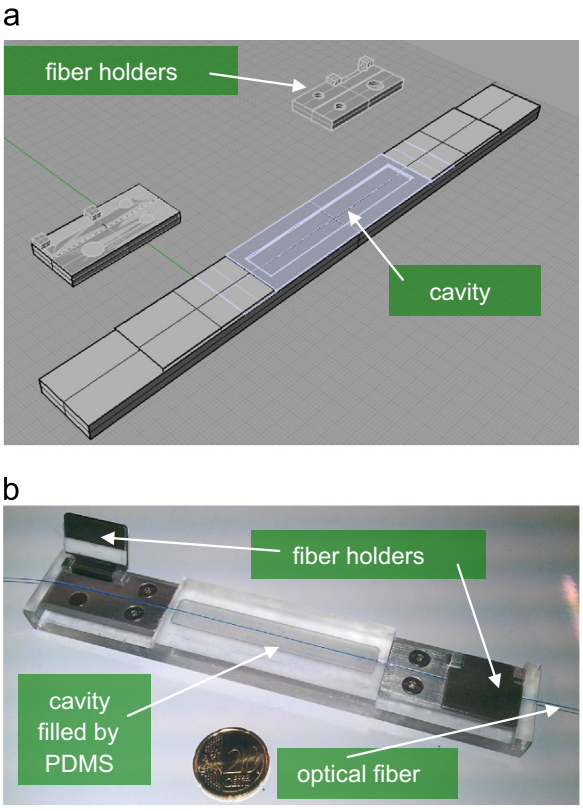

Fig. 1. (a) CAD model of the volume which is the "mold" for embedding the FBG within the PDMS. The two fiber holders are also illustrated. (b) Finished mold with the two fiber holders already screwed to it. (For interpretation of the references to color in this figure, the reader is referred to the web version of this article.)

2.2. Mold fabrication

The polymethyl methacrylate (also known as PMMA) was selected as the material for the mold because the PDMS can be easily peeled off from after the cure step. Moreover, the PMMA is a material easy to work with a CNC machine. Therefore, the mold, whose photograph is presented in Fig. 1(b), was milled using a 200 μm diameter mill in a Roland Modela MDX-20 CNC machine. The CAD model file is uploaded into the software that controls the milling and the process parameters. Then a three-axis cutting speed is set. Fig. 1(b) also shows a blue optic fiber with the correspondent FBG already embedded in the mold cavity. A single person can easily insert the optic fiber with the FBG, center it in the cavity, and hold it straight and in place when the two holders are clamped.

In conclusion, this mold allows the fabrication of virtually endless patches in a very simple and low resourceful way, both in materials used and process operator. Moreover, to fabricate new ones with different dimensions is very easy just having to change the parameters in the file to upload into the CNC machine. All of these features provide a simple, easy, expedite and low-cost process.

2.3. FBG embedment process in PDMS

The density of the selected PDMS is 965 kg m^{-3}, whereas the volume of the mold cavity is 585 mm^3. This means that in accordance with the fact the density [kg m^{-3}] to be given by the ratio between the mass [kg] with relation to the volume [m^3] (e.g., density = mass/volume), the mass of the PDMS and the curing agent needed to completely fill the mold and embed the FBG is 0.565 g. It must be noted that 10% of this value is constituted by the curing agent supplied with the PDMS. Once the cavity is filled, it is placed inside an oven for 1 h at the temperature of 85 °C for the curing step of the fabrication process. The thermal treatment was required because the transition from the liquid into the solid phase could take at least 48 h, when performed at the environmental temperature [20].

3. Measurement

The proposed flexible sensor is based on a single optical Fiber Bragg Grating (FBG) with a resonance on a specific wavelength. Essentially, the FBG is a periodic variation of the refraction index along the fiber axis, which was obtained by adequately exposing the fiber to intense ultra violet (UV) light [21]. Further details about the technology used for writing periodic grating into the core of optical fibers can be found on excellent papers and review articles [22–27]. However and to keep the key-idea of FBGs, the length of the gratings is in the order of a few millimeters and is characterized by a narrowband resonance spectral reflection [22]. This makes the structure to work as a reject-band filter, reflecting back the spectral component, λ_B [nm], which satisfies the Bragg condition (given by Eq. (2)) and transmitting the remaining components. The Bragg wavelength is given by [28–31]

$$\lambda_B = 2n_{eff}\Lambda \tag{1}$$

where Λ [nm] is the grating pitch and n_{eff} is the effective refraction index of the fiber core. The wavelength shift, $\Delta\lambda_B$ [nm], of a FBG sensor subject to a physical disturbance is given by [32]

$$\frac{\Delta\lambda_B}{\lambda_B} = (1-\rho_e)\Delta\varepsilon + (\alpha+\xi)\Delta T \tag{2}$$

where ρ_e, $\Delta\varepsilon$, α, ξ, and ΔT are the effective photoelastic constant, the axial strain, the thermal expansion, the thermal optic coefficient and the temperature shifts, respectively. The ratio in the first term of Eq. (2) expresses the strain effect on an optical fiber. This quantity corresponds to a change in the grating spacing and the strain-optic induced change in the refractive index. The temperature sensing is related with the second term of the expression. For the specific case of a 1550 nm FBG inscribed into a silica fiber, the wavelength sensitivities with respect to changes in the axial strain and in the temperature are typically ≈ 1 pm $\mu\varepsilon^{-1}$ and ≈ 13 pm °C^{-1}, respectively [32]. Therefore, it is mandatory to proceed with the temperature offset compensation for only measuring strains. An additional FBG is used and not embedded into the carrier and simultaneously is kept floating with respect to the places where strains take place for avoiding the occurrence of cross couples between the strain and the temperature components. Moreover, it is of major importance to provide a rigid support to fix this additional FBG to avoid couplings from undesirable strains. This simple solution is effective because makes possible to measure the temperature in an independent way, when both the magnitudes of the strain and temperature vary simultaneously.

A measurement setup was assembled to evaluate the FBG versus a commercial simple flex sensor (Sparkfun SEN-08606) with a flat resistance of 10 kΩ as a reference to compare values and for benchmarking purposes. Two flex sensors (which change linearly its resistance value when deflected) were connected into a Wheatstone bridge in opposite sides for doubling the measured range value and correspondent precision. Both sensors were used to measure bends and flexes physically actuated with a motion device. For the characterization, the embedded FBG was applied to a flexible polymer substrate with an adhesion compound. Adjacent to the FBG, two flex sensors for determining the actual curvature of the substrate were applied, seen in Fig. 2. The wavelength versus the curvature (and then, versus the elongation) variation was obtained during the measurements.

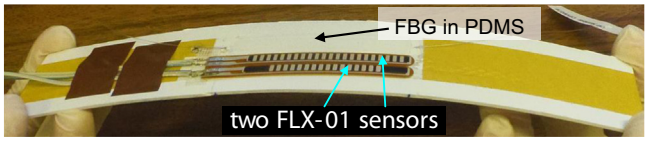

Fig. 2. A functional prototype of the flexible sensor with two flex sensors fixed on a flexible polymer substrate.

The optical interrogation system was mounted in order to provide a set of requirements for this kind of acquiring systems: multiplexing, scalability, integration, mobility, data transfer and cost effective. The optical interrogation system is composed by an optical source, an optical circulator, by one or more FBGs (naturally, all presenting different resonance wavelengths), and by the optical detector. It is recommended an optical source with broadband, therefore, it was selected a series of Superluminiscent LEDs to generate a light beam with a spectrum in the range between 1530 and 1570 nm and a maximal power of 8 mW.

The FBGs were produced in such a way that the gratings were written in hydrogen loaded standard telecommunication fiber corning SMF28e+ using the phase mask technique and a pulsed Excimer Laser. The gratings were written in order to resonate at the 1552.37 nm wavelength.

The optical circulator was used for separating a "single" reflected component from the injected spectrum, and presented a pass-band characteristic between 1525 and 1565 nm. Additionally, the optical circulator presents a typical insertion loss of 0.7 dB (meaning that the loss does not exceed 15% of the totality of the power), a maximum polarization loss of 0.2 dB (e.g., a maximum of 5%) and an isolation between the reverse and the direct inputs of at least 50 dB (the leaking between the reverse and direct inputs is smaller than 0.01%).

The optical detector can resolve the spectrum of optical signals between 1529 and 1561 nm with a precision of 1 pm for optical powers larger than -20 dB m. The optical detector also presents a dynamic range of 30 dB and a maximum wavelength drift of 2 pm $^{\circ}C^{-1}$.

3.1. Static behavior

Fig. 3 illustrates the assembled setup, which is composed by the dynamometer model H100KS from the manufacturer Hounsfield, available in the textile engineering department, by the optical components (e.g., the flexible sensor and optical interrogation system) and by a personal computer. The dynamometer was used for applying vertical forces from the top toward the bottom direction, in order to bend the polymeric substrate at the constant displacement rate (the vertical motion was programmed to shift 10 mm at the speed of 1 mm for each 12 s).

In order to plot the FBG wavelength versus curvature, several tests were performed. The test started with the Bragg wavelength of λ_B=1552.37 nm, which corresponds to a linear/horizontally stetched FBG position, with 0° of curvature. The graph on top of Fig. 4 shows the wavelength shift $\Delta\lambda$ [nm] from the Bragg wave length λ_B [nm] (e.g., $\Delta\lambda=\lambda-\lambda_B$) that was measured in terms of the axial displacement ε_Δ [%]. The elongation ε_Δ is the percentual strain Δd with relation to the rest length d_0 of the FBG, given by $\varepsilon_\Delta=\Delta d/d_0\times 100\%$.

The graph on bottom of Fig. 4 shows the mean values $\Delta\lambda_{mean}$ of the seven sets of measurements and the curve fitting $\Delta\lambda^*$ obtained from the mean value. The error lines in the mean values plot were calculated from repeated measurements. Rather than two error sets, two error lines were obtained because the data was acquired at a relatively high frequency f_s [Hz] of 588 samples per second. The seven acquisitions used this frequency f_s and took 120 s. For a set of

Fig. 3. A general view of the measurement setup or getting the static behavior.

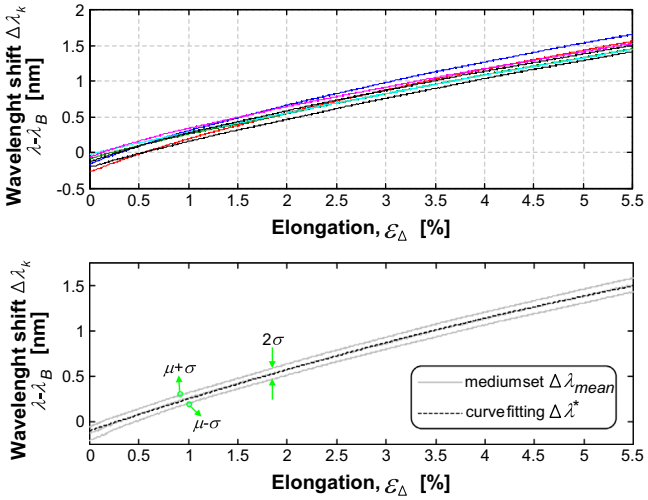

Fig. 4. Plot with the measured curvatures of the substrate, showing the wavelength shifts with relation to the FBG displacement in the axial direction.

N measurements, $\Delta\lambda_k$, $k\in\{1,2,\ldots,N\}$, the center and the half-length of the respective line is equal to medium value and to standard deviation. The standard deviations σ_k [nm] were calculated for all individual values $\Delta\lambda_k$ for a given axial displacement $\varepsilon_{\Delta(k)}$ taking into account the mean value μ_k for this same angle. The values for the medium and the standard deviation are calculated as follows: $\mu=(\Delta\lambda_1+\Delta\lambda_2+\cdots+\Delta\lambda_N)/N$, $\sigma=[(\Delta\lambda_1-\mu)^2+(\Delta\lambda_2-\mu)^2+\cdots+(\Delta\lambda_N-\mu)^2/N]^{1/2}$. The measurements revealed standard deviations between 78.40×10^{-3} and 55.76×10^{-3} nm with a mean value of 6.17×10^{-3} nm. The curve fitting $\Delta\lambda^*$ in terms of strain $\varepsilon_{\Delta(k)}$ whose shape is showed on bottom of Fig. 4 was approximated by this polynomial function of second order

$$\Delta\lambda^* = A\varepsilon_\Delta{}^2 + B\varepsilon_\Delta + C \tag{3}$$

with $A=-13.22\times10^{-3}$, $B=362.76\times10^{-3}$ and $C=99.39\times10^{-3}$. At naked eye, it is possible to observe that these two last shapes are very close to the measured ones on top. A more precise statistical test has been done for validating these results, e.g., it was calculated the individual correlation coefficients ρ_k of the curve fitting $\Delta\lambda^*$ with relation to each of the individual plots $\Delta\lambda_k$, whose values are {0.9999, 0.9996, 0.9999, 0.9998, 0.9994, 0.9997, and 0.9998}. The correlation coefficients ρ of the curve fitting $\Delta\lambda^*$ with relation to the plot $\Delta\lambda_{mean}$ with medium values was also calculated and resulted on $\rho=0.9999$. These indicators confirm the use of Eq. (3) to fully characterize the sensor's behavior. Moreover, the relation between $\Delta\lambda^*$ and ε_Δ can be approximated by a linear function because the first order coefficient

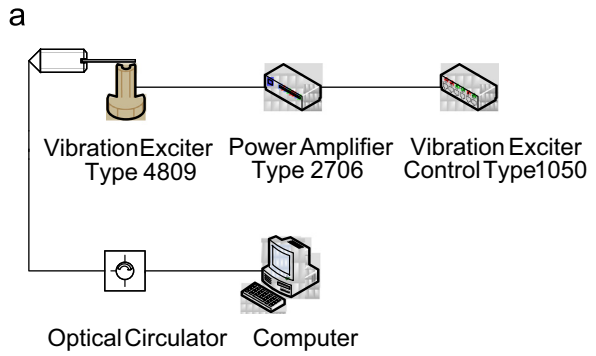

Fig. 5. (a) The block diagram of the measurement setup using in the characterization of the dynamical behavior and (b) the respective photography.

B in Eq. (3) is more than one order of magnitude above the second order coefficient *A*.

3.2. Dynamic behavior (single frequency excitation)

Several different tests were performed to evaluate the precision, consistency and the variation of the two different sensors, considering the amplitude and frequency of the input signal. In order to analyze the FBG sensor dynamic response under fluctuating loads, the test setup in the Fig. 5 was assembled. This setup is capable of producing sinusoidal signals with variable frequency and amplitude, and translates them into movement. A programmable vibration exciter (Brüel & Kjaer Vibration Exciter Control Type 1050) is responsible for creating an output signal waveform. The generated function is amplified by a power amplifier (Brüel & Kjaer Power Amplifier Type 2706) which in turn drives a vibrational shaker (PM Vibration Exciter Type 4809). An accelerometer (Brüel & Kjaer Accelerometer Type 4371) is used with the vibration exciter in a closed loop feedback circuit to control the vibrational shaker displacement.

One end of the substrate was fixed in a vise while the opposite one was attached to the shaker axle in a pivot point. This configuration enabled bending forces to be applied evenly on the flexible substrate containing the sensors.

Numerous tests were performed for different values of frequency and amplitude. Fig. 6 presents the FBG's response to six sinusoidal signals of 1.05 Hz, but each with different amplitudes that induced peak-to-peak shaker displacements from 1 to 6 mm, correspondingly. Again, it can be observed that the FBG presents a linear dynamic response to the induced movement.

A significant number of tests were performed for sinusoidal signals with different values of frequency and amplitude (the peak-to-peak shaker displacements were varied from 1 to 6 mm on increments of 1 mm). The targeted frequencies were initially targeted to be near 1,

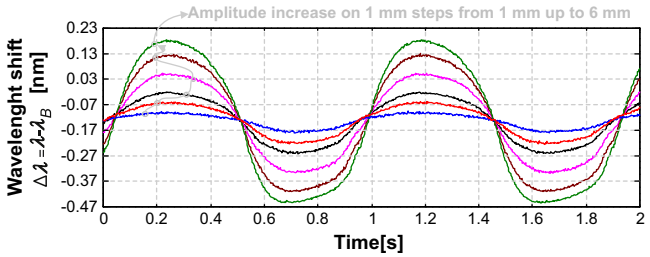

Fig. 6. The response of the FBG to six waves oscillating at the targeted frequency of 1.05 Hz for different displacements. All the signals were superimposed for allowing a better illustration of the amplitudes ranging from 1 mm to 6 mm.

5 and 50 Hz, however the signal generator used by the shaking system presented a given uncertainty. This resulted in the existence of a frequency error, given by the difference between the targeted frequency f_{target} and the main peak's position f_{main}. The actual generated frequencies were measured to be 1.05, 5.27 and 61 Hz, corresponding to a relative error ε_f of approximately 5%, 5.32% and 22%, respectively. Additionally, the relative error of the frequency in the signal generator is given by $\varepsilon_f = (f_{main}\text{-}f_{target})/f_{target} \times 100$ [%] and increases with the frequency. The main peaks f_{main} and thus, the relative error dependence with the targeted frequency f_{target} were estimated to be $\varepsilon_f \approx 4.65 + 0.35 f_{target}$%. Fig. 7 shows the frequency spectral distribution of the signals with the shaking system oscillating at 1.05, 5.27 and 61 Hz with amplitudes. These spectral distributions were obtained by applying a FFT to the six time discrete samples. It can be observed, in each of the three FFTs presented, the existence of the dominating peak at the correspondent frequency (1.05, 5.27 and 61 Hz). Again and when looking from the fundamental component point of view, the FBG presents a linear dynamic response to the induced movement. Therefore, this makes this sensor suitable for resolving strains with high resolution.

3.3. Dynamic behavior (linear varying excitation)

With the objective of obtaining a more complete dynamic characterization, a variation, in a continuous manner, of the oscillating frequency was performed. In this sense, the spectrogram showed in Fig. 8 was calculated. It is possible to clearly observe a variation of the oscillating frequency along the time (marked as an oblique line with amplitude around 20 dB and going from approximately 3 to about 11 Hz having its values calculated in the initial and final instants, respectively). The spectrogram allows observing other frequency peaks of lower amplitude at higher frequencies than the oscillating one (the most intense of all is located at twice the fundamental one). These frequencies are easily identified at naked eye, when considering the time versus the frequency range of Fig. 8. It is also possible to observe that these frequencies are located in the second, third and fourth harmonics of the fundamental that was generated by the shaker.

Fig. 9(a) shows few portions of the acquired signal with the number of samples equal to the length of the window used in the FFT. The chart is divided in three equal parts having also the size of the length of the window used in the FFT. The first third of the chart is made using the values of the acquired signal from 0 to 2.56 s; the second third corresponds to the 51.16–53.72 s range and the last third represents the signal from 102.32 to 104.88 s.

Fig. 9(b) shows the spectrums of each of the three parts that compose Fig. 9(a). It is possible to confirm the equidistance between the main peaks. This distance is due to the fact that the oscillating frequency varies linearly along the time and the three parts are temporally equidistant one from the other. As described before, the first, second and third parts of the chart begin at 0, 51.16 and 102.32 s, respectively (at an equal distance of 51.16 s between them). Although

in each spectrum there are secondary peaks, their amplitudes are well below the main peak therefore can be neglected.

The non-linearity inherent to the shaking systems and to the supporting cantilever is transmitted into the FBG. However, the high sensitivity of this sensor allows their detection and quantification. A figure-of-merit D [dB] can quantify the degree introduced by the non-linear components of the system. This is a numerical indicator and can be defined taking into account the amplitudes A_1 [dB] of the main peak at the fundamental frequency with relation to the higher secondary peak A_2 [dB]. This quantity takes the form of a spectral distortion and is given by $D=A_1-A_2$ [dB].

Table 1 summarizes few values for D, where it is possible to observe that the secondary with the higher amplitude is always 20 dB (one order of magnitude below or ten times smaller) below the main peak at the fundamental frequency.

3.4. Behavior to temperature changes

The thermal behavior of this flexible sensor was also obtained. As showed in Fig. 10(a), the flexible sensor prototypes were glued

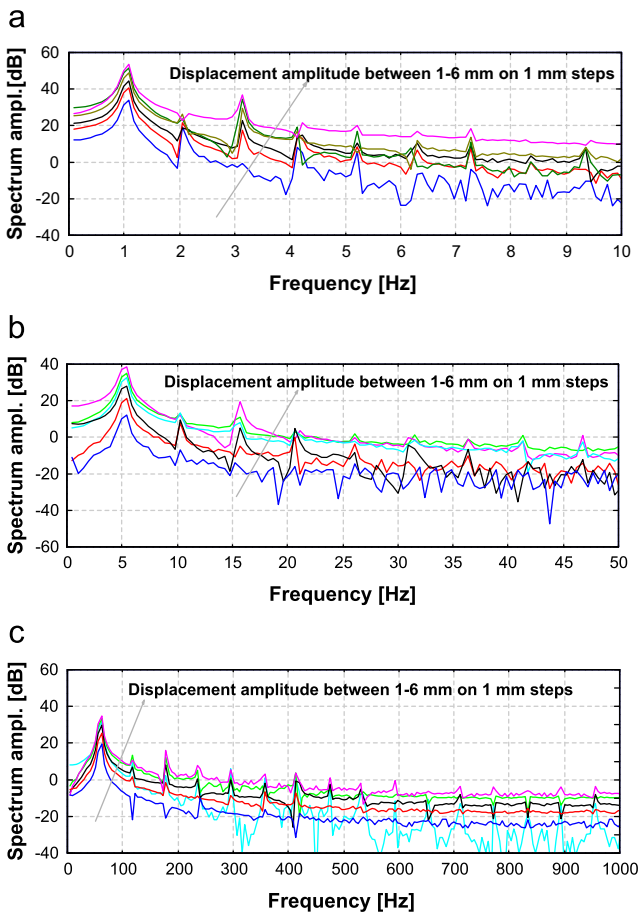

Fig. 7. Frequency spectral distribution of the acquired signals from the FBG in response esponse to multiple periods with the shaker oscillating at (a) 1.05 Hz, (b) 5.32 Hz and (c) 61 Hz. Each plot shows the spectrum overlapping for the six different amplitudes in 1 mm increments.

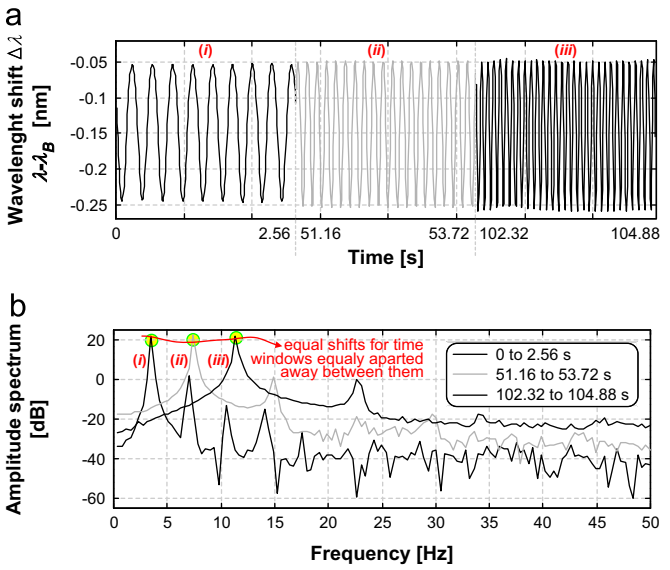

Fig. 9. (a) Time and (b) frequency domain representations of three portions of the acquired signal. It must be noted that the duration of each portion is equal 2.56 s. For each portion: (i) beginning of the acquired signal (starting at 0 s), (ii) half acquisition time (starting at 51.16 s), and (iii) final of the acquired signal (starting at 102.32 s).

Table 1
Few values of D for the three portions of the acquired signal, for the both signals (time and frequency domains) showed in Fig. 9.

Signal portion	Time limits [s]	Main peak A_1 [dB]/f_1 [Hz]	Secondary peak A_2 [dB]/f_2 [Hz]	D [dB]
#1	0–2.56	22.08/3.51	2.18/7.02	19.90
#2	51.32–53.72	22.33/7.42	1.52/14.84	20.81
#3	102.32–104.88	21.90/11.32	−0.15/22.64	22.05

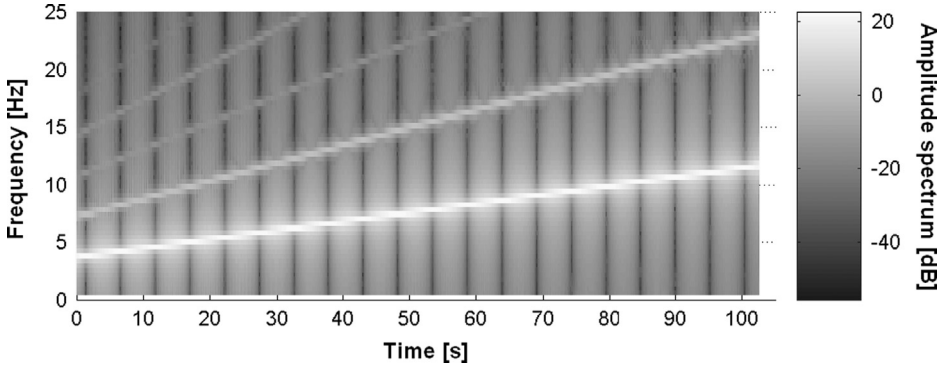

Fig. 8. Spectrogram of the acquired signal. The shaker's oscillating frequency was swept from 3 to 10 Hz during the measurement. The length of the sliding window for calculating the FFT is equal to 256 samples.

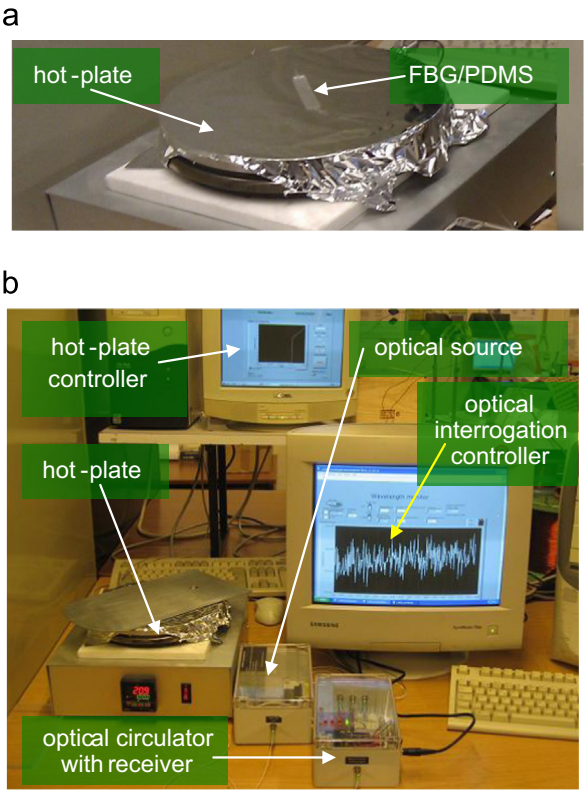

Fig. 10. (a) A zoomed photography of the flexible sensor glued into a metallic sheet made of aluminum and positioned on top of the hot-plate that was used for characterizing the thermal behavior of this flexible sensor. (b) Photography of the whole setup that was used for acquiring the thermal behavior.

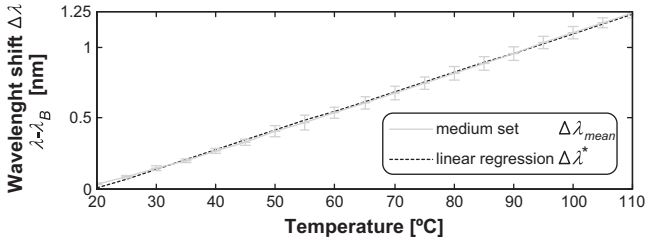

Fig. 11. Thermal behavior of this flexible sensor. $\rho(\Delta\lambda_{mean},\Delta\lambda^*)=99.95\%$.

into a metallic sheet made of aluminum, which was further placed above a hot-plate. The temperature in the surface of the heat source was swept between 20 °C and 110 °C on steps of 10 °C. The complete setup to characterize the thermal behavior of this flexible sensor is showed in the photography of Fig. 10(b).

The thermal behavior of this flexible sensor can be observed in Fig. 11. Once again, a set of seven plots were acquired under the same conditions for allowing the calculation of the standard deviations around the medium values $\Delta\lambda_{mean}$. It was followed the same procedure that was previous described to obtain the different values of μ and σ. The only difference between Figs. 4 and 11 can be explained as follows: the high number of points in Fig. 4 gives the false sensation of continuity in the $\mu+\sigma$ and $\mu-\sigma$ plots (as well as, in the plot of $\mu=\Delta\lambda_{mean}$), whereas the 19 points makes easy to identify the means and the error bars.

The Fig. 11 also shows a second plot $\Delta\lambda^*$, which was obtained after calculating the linear regression. On both plots, the temperature rising is followed by a positive deviation of the sensor reflected wavelength. However, the plot of $\Delta\lambda^*$ confirms that the obtained data tend to follow a linear fit with a correlation coefficient of $\rho=0.9995$. Additionally, the response to temperature changes of this flexible sensor, within the 20-110 °C range, was observed to follow a slope 14 pm °C^{-1}. Contrary to what found on other solutions (e.g., 100 pm °C^{-1}) [33], this value is low and very similar to which is found on raw FBGs (e.g., ≈ 13 pm °C^{-1}) [34], making optional the use of a temperature compensation mechanism. The temperature coefficient is required only in the presence of high temperature gradients. In this case, a second sensor not embedded into the PDMS and kept floating, must be used for avoiding the occurrence of cross-couples between the desired signals to acquire and the temperature component.

4. Conclusion

This paper presented a flexible sensor based on photonics for measuring strains, curvatures and vibrations. This flexible sensor is composed by a FBG embedded into PDMS. The functions of the PDMS were to serve simultaneously as physical carrier, as mechanical buffer between the surface subject to strains and as structural adhesive. In conclusion, it must be noted that major features of these flexible sensors is the high-simplicity employed on the prototype's fabrication with high reproducibility of their characteristics. Moreover, its inherent simplicity results on a lowcost fabrication process.

Acknowledgment

This work and the scholarship of Mr. José Miguel Gomes, MSc, were fully supported by the Project FCT/PTDC/EEA-ELC/109936/2009. We would like to thanks to Mr. Joaquim Jorge from the Textile Engineering Department (DET) at University of Minho for the help during the static tests with the dynamometer. The FBGs were fabricated by the FiberSensing Company SA.

References

[1] Chang-Jian S-K, Ho J-R, Cheng J-WJ. Fabrication of transparent double-walled carbon nanotubes flexible matrix touch panel by laser ablation technique. Optics and Laser Technology 2011;43(8):1371–6.
[2] Yang Q, Zhao B, Wen D. Principle and analysis of a moving double-sided mirror interferometer. Optics and Laser Technology 2012;44(5):1256–60.
[3] Fanga Z, Chen QY. A review of recent progress in lasers on silicon. Optics and Laser Technology 2013;46:103–10.
[4] Zebentout AD, Aissat AK, Bensaad Z, Zegaoui M, Pagies A, Decoster D. GaAs metal–semiconductor–metal Schottky microwave optical switches. Optics and Laser Technology 2013;47:1–3. http://dx.doi.org/10.1016/j.optlastec.2012.08.026.
[5] Cho H, Cho BC, Hong HJ, Oh E-Y, Kwon Oh-Kyong. A color local dimming algorithm for liquid crystals displays using color light emitting diode backlight systems. Optics and Laser Technology 2013;47:80–7.
[6] Stasiek J, Stasiek A, Jewartowski M, Collins MW. Liquid crystal thermography and true-colour digital image processing. Optics and Laser Technology 2006;38(4-6):243–56.
[7] Kurada S, Rankin G -W, Sridhar K. A trinocular vision system for close-range position sensing. Optics and Laser Technology 1995;27(2):75–9.
[8] Lan J, Li J, Hu G, Zeng Y. Distance estimation using a panoramic sensor based on a novel spherical optical flow algorithm. Optics and Laser Technology 2013;45:168–76.
[9] Carpi F, de Rossi D. Colours from electroactive polymers: electrochromic, electroluminescent and laser devices based on organic materials. Optics and Laser Technology 2006;38(4-6):292–305.
[10] Chen J-H, Huang X-G, He W-X, Tao J. A parallel-multipoint fiber-optic temperature sensor based on Fresnel reflection. Optics and Laser Technology 2011;43(8):1424–7.
[11] Zhen S, Chen B, Yuan L, Li M, Liang J, Yu B. A novel interferometric vibration measurement sensor with quadrature detection based on 1/8 wave plate. Optics and Laser Technology 2010;42(2):362–5.
[12] Zhou W, Dong X, Shen C, Zhao C-L, Chan CC, Shum P. Temperature-independent vibration sensor with a fiber Bragg grating. Microwave abd Optical Technology Letters 2010;52(10):2282–5.
[13] Zhou W, Dong X, Ni K, Chan CC, Shum P. Temperature-insensitive accelerometer based on a strain-chirped FBG. Sensors and Actuators A 2010;157:15–8.

[14] Antunes P, Varum H, André P. Uniaxial fiber Bragg grating accelerometer system with temperature and cross axis insensitivity. Measurement 2011;44:1–5.
[15] Zhang W, Li F, Liu Y. FBG pressure sensor based on the double shell cylinder with temperature compensation. Measurement 2009;42:408–11.
[16] Li D, Zhou Z, Ou J. Dynamic behavior monitoring and damage evaluation for arch bridge suspender using GFRP optical fiber Bragg grating sensors. Optics and Laser Technology 2012;44(4):1031–8.
[17] Melik R, Unal E, Perkgoz NK, Puttlitz C, Demir HV. Flexible metamaterials for wireless strain sensing. Applied Physics Letters 2009;95(18):1–3.
[18] Melik R, Unal E, Perkgoz NK, Santoni B, Kamstock D, Puttlitz C, et al. Nested metamaterials for wireless strain sensing. IEEE Journal of Selected Topics in Quantum Electronics 2010;16(2):450–7.
[19] Siu C-P-B, Chiao M. A microfabricated PDMS microbial fuel cell. Journal of Microelectromechanical Systems 2008;17(6):1329–41.
[20] Liu M, Sun J, Chen Q. Influences of heating temperature on mechanical properties of polydimethylsiloxane. Sensors and Actuators A 2009;151 (1):42–5.
[21] Hill K, Meltz G. Fiber Bragg grating technology fundamentals and overview. IEEE Journal of Lightwave Technology 1997;15:1263–76.
[22] Erdogan T. Fiber grating spectra. IEEE Journal of Lightwave Technology 1997;15:1277–94.
[23] Hill KO, Malo B, Bilodeau F, Johnson DC. Photosensitivity in optical fibers. Annual Reviews of Materials Science 1993;23:125–57.
[24] Morey WW, Ball GA, Meltz G. Photoinduced Bragg gratings in optical fibers. Optics and Photonics News 1994;5:8–14.
[25] Campbell RJ, Kashyap R. The properties and applications of photosensitive germanosilicate fiber. International Journal of Optoelectronic Engineering 1994;9:33–57.
[26] St. P, Russell J, Archambault J-L, Reekie L. Fiber gratings. Physics World 1993:41–6.
[27] Bennion I, Williams JAR, Zhang L, Sugden K, Doran NJ. UV-written in-fiber Bragg gratings. Optical and Quantum Electronics 1996;28:93–135.
[28] Kersey AD, Davis MA, Patrick HJ, LeBlanc M, Koo KP, Askins CG, et al. Fiber grating sensors. IEEE Journal of Lightwave Technology 1997;15:1442–63.
[29] Othonos A. Fiber Bragg gratings. Review of Scientific Instruments 1997;68:430–341.
[30] Rao YJ. In-fiber Bragg grating sensors. Measurement Science and Technology 1997;8:355–75.
[31] Moreira PJ, Ferreira LA, Santosm JL, Farahi F. Dynamic range enhancement in fiber Bragg grating sensors using a multimode laser diode. IEEE Photonics Technology Letters 1999;11(6):703–5.
[32] Wei C-L, Lai C-C, Liu S-Y, Chung W, Ho T, Ho S, et al. A fiber bragg grating sensor system for train axle counting. IEEE Sensors Journal 2010;10:1905–12.
[33] Silva AF, Goncalves F, Ferreira LA, Araujo FM, Mendes PM, Correia JH. A smart skin PVC foil based on FBG sensors for monitoring strain and temperature. IEEE Transactions on Industrial Electronics 2011;58(7):2728–35.
[34] Bozolan A, Gerosa RM, de Matos CJS, Romero MA. Temperature sensing using colloidal-core photonic crystal fiber. IEEE Sensors Journal 2012;12 (1):195–200.